



Published in final edited form as:

*Phys Rev Fluids*. 2019 April ; 4(4): . doi:10.1103/PhysRevFluids.4.043103.

## Dynamics of deformable straight and curved prolate capsules in simple shear flow

Xiao Zhang<sup>1</sup>, Wilbur A. Lam<sup>2,3,4,5</sup>, Michael D. Graham<sup>1,\*</sup>

<sup>1</sup>Department of Chemical and Biological Engineering University of Wisconsin-Madison, Madison, WI 53706-1691

<sup>2</sup>Wallace H. Coulter Department of Biomedical Engineering Emory University and Georgia Institute of Technology, Atlanta, GA 30332

<sup>3</sup>Department of Pediatrics, Division of Pediatric Hematology/Oncology, Aflac Cancer and Blood Disorders Center of Children's Healthcare of Atlanta Emory University School of Medicine, Atlanta, GA 30322

<sup>4</sup>Winship Cancer Institute Emory University, Atlanta, GA 30322

<sup>5</sup>Parker H. Petit Institute of Bioengineering and Bioscience Georgia Institute of Technology, Atlanta, GA 30332

### Abstract

This work investigates the motion of neutrally-buoyant, slightly deformable straight and curved prolate fluid-filled capsules in unbounded simple shear flow at zero Reynolds number using direct simulations. The curved capsules serve as a model for the typical crescent-shaped sickle red blood cells in sickle cell disease (SCD). The effects of deformability and curvature on the dynamics are revealed. We show that with low deformability, straight prolate spheroidal capsules exhibit tumbling in the shear plane as their unique asymptotically stable orbit. This result contrasts with that for rigid spheroids, where infinitely many neutrally stable Jeffery orbits exist. The dynamics of curved prolate capsules are more complicated due to a combined effect of deformability and curvature. At short times, depending on the initial orientation, slightly deformable curved prolate capsules exhibit either a Jeffery-like motion such as tumbling or kayaking, or a non-Jeffery-like behavior in which the director (end-to-end vector) of the capsule crosses the shear-gradient plane back and forth. At long times, however, a Jeffery-like quasiperiodic orbit is taken regardless of the initial orientation. We further show that the average of the long-time trajectory can be well approximated using the analytical solution for Jeffery orbits with an effective orbit constant  $C_{\text{eff}}$  and aspect ratio  $\ell_{\text{ff}}$ . These parameters are useful for characterizing the dynamics of curved capsules as a function of given deformability and curvature. As the capsule becomes more deformable or curved,  $C_{\text{eff}}$  decreases, indicating a shift of the orbit towards log-rolling motion, while  $\ell_{\text{ff}}$  increases weakly as the degree of curvature increases but shows negligible dependency on deformability. These features are not changed substantially as the viscosity ratio between the inner and outer fluids is changed from 1 to 5. As cell deformability, cell shape, and cell-cell

\*Corresponding author. mdgraham@wisc.edu.

interactions are all pathologically altered in blood disorders such as SCD, these results will have clear implications on improving our understanding of the pathophysiology of hematologic disease.

---

## I. INTRODUCTION

A healthy human red blood cell (RBC) is a fluid-filled biconcave discoid with an incompressible membrane comprised of a fluid lipid bilayer tethered to an elastic spectrin network [1]. In the past decades, experimental and computational studies have revealed a rich spectrum of dynamical modes for RBCs in shear flow over a vast domain of parameter space in terms of membrane mechanics of RBC and flow conditions [2–11]. In pathological cases where normal blood flow is altered, the dynamics of diseased RBCs can be very different from those of healthy ones because of differences in cell properties. In sickle cell disease (SCD), for example, the intracellular polymerization of sickle hemoglobin (HbS) leads to an abnormality in the shape of individual sickle RBCs, but a large variation in cell morphology has been revealed within the population of sample cells. Using diffraction phase microscopy, Byun *et al.* [12] performed optical measurement for individual sickle RBCs, and classified them into echinocytes, discocyte, and the typical crescent-shaped irreversibly sickled cells (ISCs) based on their morphological features. Numerical simulations have also enhanced the understanding of the nature of HbS polymer fiber formation and growth [13–17], and corroborated experimental observations of considerable heterogeneity in cell morphologies [13, 15, 18]. In addition, using various techniques for the characterization of cell membrane mechanics, a general decrease in deformability of sickle RBCs compared to that of normal RBCs has been determined; the extent of membrane stiffening varies greatly depending on the states and conditions of individual sickle RBCs [12, 19–22]. The decrease in membrane deformability for non-ISCs (namely, all sickle RBCs other than ISCs [23]) is found to be slight under oxygenated conditions [20], but substantial upon deoxygenation [19], while ISCs exhibit much lower deformability than non-ISCs in both states [19–21].

All these variations for individual sickle RBCs mentioned above pose challenges to understanding the dynamics of sickle RBCs in flow. The present work aims to take a step toward this understanding by performing a systematic computational investigation of the dynamics of a model sickle cell in simple shear flow and illustrating the effects of initial orientation, membrane deformability and curvature of the cells on their dynamical motions.

A sickle RBCs might be thought of as a perturbed case of a deformable spheroidal capsule, and this is how we model it below, so here we review relevant literature on this class of particles in flow. The canonical example of this class is a simple rigid neutrally-buoyant spheroid, whose motion in simple shear flow at zero Reynolds number can be described by trajectories known as Jeffery orbits [24]. During flow the center-of-mass position of the spheroid remains on its initial streamline with no drift in any direction, while its major axis of symmetry traces out a closed periodic orbit depending on its initial orientation. Each orbit corresponds to a specific non-negative orbit constant  $C$ , so the quantity  $C_b = C/(1 + C)$  is bounded by zero and one. When  $C = C_b = 0$ , the particle rolls with its major axis aligned with the vorticity direction, while  $C_b = 1 (C = \infty)$  corresponds to a pure tumbling motion in the shear plane. For any intermediate value of  $C_b$ , the major axis of the particle undergoes a

so-called kayaking motion. Bretherton [25] later showed that Jeffery's solution can be applied to describe the dynamics of any axisymmetric rigid body with fore-aft symmetry.

Jeffery orbits are highly degenerate because of the combination of symmetry, Stokes flow reversibility and rigidity. Many efforts have been made to examine the behaviors of particles immersed in shear flow when these conditions are not strictly satisfied. For example, large changes in the orbital behaviors were observed in a number of studies when deviations from axisymmetric geometry were introduced. Hinch and Leal [26] derived the equations for the motion of general (non-axisymmetric) ellipsoids in simple shear flow, observing that the motion of a triaxial ellipsoid with comparable axes has doubly periodic (quasiperiodic) dynamics. For triaxial ellipsoids with one axis significantly longer than the other two, Yarin *et al.* [27] numerically observed chaotic behavior and proposed an analytical theory to explain the onset of this chaotic motion. Subramanian and Koch [28] found through a theoretical investigation that when small but finite inertia was considered, the degeneracy of Jeffery orbits is broken and particular orbits become attractors for the long-time dynamics. In particular, they predicted that the attractor of a slightly prolate spheroid would evolve from the shear plane via an intermediate orbit towards the vorticity axis, as the ratio of particle density to fluid density decreased. Using numerical simulations, Mao and Alexeev [29] examined the effects of fluid inertia and particle inertia on the dynamics of a solid spheroidal particle in simple shear flow, finding that at zero Reynolds number, particle inertia would cause the orientation of a prolate spheroid to drift toward a tumbling orbit in the shear plane, but the drift direction would change from in-plane tumbling to rolling around the vorticity axis when the Reynolds number exceeded a critical value.

Many computational studies have also addressed how the degeneracy of Jeffery's solution is broken in the presence of deformability as for capsules and solid elastic particles. Here capillary number, which represents the ratio of viscous stresses to elastic restoring stresses on the particle, characterizes the deformability of the particle. We mainly focus on the works regarding prolate particles which are of direct pertinence to the present paper. Most numerical studies regarding prolate capsules focused on the case where the inner and outer fluids have the same viscosity. Walter *et al.* [30] investigated the behavior of a prolate capsule in simple shear flow with the revolution axis of the capsule initially lying in the shear plane. The membrane was modeled as a hyperelastic surface with no bending resistance. They observed that the prolate capsule took a rigid-body like tumbling motion at low shear rate (i.e. capillary number), and exhibited a fluid-like behavior termed swinging at high shear rate in which the membrane rotates around its deformed shape and the capsule elongation and orientation oscillate in shear flow. This tumbling-to-swinging transition was even found for a spheroidal compound capsule consisting of a spherical inner capsule enclosed by a spheroidal outer capsule at vanishing viscosity mismatch by increasing the inner capsule size alone [31]. Out-of-shear plane dynamics of prolate capsules have also gained an increasing understanding in recent years. Dupont *et al.* [32] and Cordasco and Bagchi [33] numerically studied three-dimensional orbital dynamics of isolated prolate capsules in simple shear flow with off-plane initial orientations, and revealed rich dynamics of the capsules irrespective of the initial orientation. In Dupont *et al.* [32], the capsule membrane was modeled as an isotropic hyperelastic surface with shear elasticity and area dilatation described by either the Skalak law [34] or the neo-Hookean law and in the absence

of bending rigidity. They showed that at low and high capillary number regimes, the dynamics of a prolate capsule in Stokes flow converge towards a rolling motion about the vorticity axis and an oscillating-swinging motion about the shear plane as the stable orbit, respectively, and a wobbling motion in which the capsule precesses around the vorticity axis is taken at equilibrium at intermediate capillary number. This qualitative transition of motions, characterized by the change in the elastic energy stored in the membrane, was generally observed in the parameter regimes considered in this work regardless of the aspect ratio of the capsule or the membrane law. Later Cordasco and Bagchi [33] incorporated bending stiffness into a Skalak membrane for a prolate capsule with zero spontaneous curvature, and observed a procession-to-kayaking (oscillating-swinging) transition with increasing capillary number similar to the findings by Dupont *et al.* [32]. Solid elastic particles have also been studied [35, 36]. Gao *et al.* [35] theoretically predicted two in-plane dynamical modes for a neo-Hookean elastic spheroidal particle immersed in shear flow, namely trembling (similar to swinging for capsules) and tumbling, depending on the shear rate, elastic shear modulus and asphericity of the initial shape. These two regimes of motion were later observed in the numerical simulations by Villone *et al.* [36]. These authors also revealed that a particle initially oriented out of the shear plane evolved in time towards in-plane trembling or tumbling, which differs from the stable orbits for prolate capsules observed by Dupont *et al.* [32] and Cordasco and Bagchi [33]. Despite all these promising results, none of the studies to date regarding deformable spheroidal particles, however, have ever considered any distortion to the original shape such as curvature, which has formed one motivation of the present work.

A limited number of studies have addressed the dynamics of curved particles such as sickle-shaped cells. Wang *et al.* [37] simulated the motion of isolated rigid slightly curved fibers in simple shear flow at zero Reynolds number. As with triaxial ellipsoids, quasiperiodic orbit dynamics are sometimes observed. More importantly, for some initial orientations the fibers drift in the gradient direction as a result of the combined effects of the so-called “flipping, scooping, and spinning” motions. The drift rate strongly depends on the initial orientation, aspect ratio, and curvature of the fibers – in particular drift only occurs for fibers of high aspect ratio. Crowdy [38] derived a dynamical system governing the motion of a curved rigid two-dimensional circular-arc fiber in simple shear flow, and the analytical solutions of this dynamical system display the “flipping” and “scooping” motions observed in [37]. Only a small number of numerical studies have addressed the behavior of sickle cells *per se*. Examples are [39–41], in which simulations were performed to investigate and quantify the heterogeneous adhesive interaction between sickle RBCs and the endothelium during flow, and the influence of cell morphologies and membrane rigidities. The aim of these studies was to shed light on the vasoocclusion crisis associated with SCD. None of these studies have focused on the fundamental dynamics or orbital behavior of single sickle cells in shear flow.

The aim of the present study is to take a first step toward understanding the dynamics of sickle cells in blood flow, by characterizing the dynamics of a model sickle cell in shear flow and examining this behavior in the context of what we know about the dynamics of other prolate objects in flow. Specifically, we investigate the dynamics of single straight and curved prolate capsules in unbounded simple shear flow at zero Reynolds number and

discuss the effects of initial orientation, membrane deformability, and degree of curvature on their dynamics. The rest of the paper is organized as follows: in Section II we present the model for sickle RBCs and the numerical algorithm employed to obtain the fluid field, followed by a validation of our model and numerical simulation; in Section III we provide detailed results and discussion on the dynamics of single straight and curved prolate capsules; lastly, concluding remarks are presented in Section IV.

## II. MODEL FORMULATION

### A. Model and discretization

We consider an isolated neutrally-buoyant fluid-filled deformable capsule with a straight or curved prolate rest shape in unbounded simple shear flow (FIG. 1). The shear rate is  $\dot{\gamma}$ , and the undisturbed flow velocity is given as  $\mathbf{u}^\infty = (\dot{\gamma}y, 0, 0)$ . Both the suspending fluid and the fluid inside the capsule are assumed to be incompressible and Newtonian, and the viscosity ratio between the fluids inside and outside the capsule is  $\lambda$ . The prolate spheroidal shape of the capsule derives from polar stretching and equatorial compression of a spherical capsule with radius  $s$  centered at the origin. The equation for this transformation is given

$$\mathbf{x}^p = \begin{pmatrix} c/s & 0 & 0 \\ 0 & a/s & 0 \\ 0 & 0 & a/s \end{pmatrix} \cdot \mathbf{x}^s, \quad (1)$$

where  $\mathbf{x}^s$  and  $\mathbf{x}^p$  are the positions of a point on the membrane of the original spherical capsule and the mapped point on the membrane of the resulting prolate spheroidal capsule with a polar radius  $c$  and an equatorial radius  $a$  (aspect ratio  $r_p = c/a > 1$ ). The resulting prolate spheroidal capsule thus aligns with the  $x$  axis. To generate a curved capsule, we then impose a quadratic unidirectional displacement of membrane points perpendicular to the polar axis of the prolate spheroidal capsule (here in the  $y$  direction),

$$x_1^c = x_1^p, \quad (2a)$$

$$x_2^c = x_2^p - k \left[ x_1^p - \frac{1}{2}(x_1^{pl} + x_1^{pr}) \right]^2, \quad (2b)$$

$$x_3^c = x_3^p, \quad (2c)$$

where  $\mathbf{x}^{pl}$  and  $\mathbf{x}^{pr}$  are the positions of the two ends (left- and right-most membrane points) of the prolate spheroid, and  $\mathbf{x}^c = (x_1^c, x_2^c, x_3^c)$  is the position of a membrane point of the resulting curved prolate capsule mapped with the membrane point of the prolate spheroid at position  $\mathbf{x}^p = (x_1^p, x_2^p, x_3^p)$ ;  $k$  has units of inverse length, which can be nondimensionalized by  $c$  to define the degree of curvature  $K = kc$ .

The instantaneous orientation of a curved prolate capsule is defined by two unit vectors, namely  $\mathbf{p}$  and  $\mathbf{n}$ . The vector  $\mathbf{p}$  is the normalized end-to-end vector that connects the left- and

right-most membrane points of the capsule. In this work, the midpoint of the  $\mathbf{p}$  vector of the capsule is initially placed at the origin of the unbounded domain. To define  $\mathbf{n}$ , we first mark a membrane point  $\mathcal{A}$  lying in the plane of symmetry of the capsule that contains  $\mathbf{p}$ . The vector  $\mathbf{n}$  is then uniquely defined as the unit vector passing through  $\mathcal{A}$  and perpendicular to  $\mathbf{p}$  that bisects  $\mathbf{p}$  when the capsule is not deformed, as illustrated in FIG. 1. Note that for a deformed capsule, the intersection of  $\mathbf{n}$  and  $\mathbf{p}$  can be off-center of  $\mathbf{p}$ . In this work, initial conditions are chosen so that  $\mathbf{p}$  is initially in the  $x$ - $z$  plane, and the initial angle between  $\mathbf{p}$  and the  $x$  axis is denoted as  $\alpha$ . The initial angle between  $\mathbf{n}$  and its projection  $\mathbf{n}'$  onto the  $x$ - $z$  plane is  $\beta$  (note that  $\mathbf{n}' \perp \mathbf{p}$ ). Thus the initial orientation of the capsule is given by  $\alpha$  and  $\beta$ . For example,  $[\alpha, \beta] = [0, \pi/2]$  means that the capsule is initially in the  $x$ - $y$  plane with  $\mathbf{p}$  aligned with the  $x$  axis and  $\mathbf{n}$  with the  $y$  axis. If the capsule is not curved, then  $\beta$  is irrelevant to its orientation and dynamics.

The total energy  $E$  of the capsule membrane  $S$  is given as:

$$E = \frac{K_B}{2} \int_S (2\kappa_H + c_0)^2 dS + \overline{K_B} \int_S \kappa_G dS + \int_S W dS, \quad (3)$$

where  $K_B$  and  $\overline{K_B}$  are the bending moduli, and  $W$  is the shear strain energy density;  $\kappa_H$  and  $\kappa_G$  are the mean and Gaussian curvature of the membrane surface, respectively;  $c_0 = -2H_0$  is the spontaneous curvature,  $H_0$  being the mean curvature of the spontaneous shape. In this equation, the first two terms represent the Canham-Helfrich bending energy [42, 43], and the third term corresponds to the shear strain energy stored in the capsule membrane. To describe the behavior of the capsule membrane in response to the in-plane shear elastic force, a membrane model by Skalak *et al.* [34] is utilized, in which the shear strain energy density  $W$  is given by

$$W_{\text{SK}} = \frac{G}{4} [(I_1^2 + 2I_1 - 2I_2) + C_a I_2^2], \quad (4)$$

where  $G$  is the in-plane shear modulus of the membrane, and  $C_a$  characterizes the energy penalty for area change of the membrane. The strain invariants  $I_1$  and  $I_2$  are functions of the principal stretch ratios  $\lambda_1$  and  $\lambda_2$ , defined as

$$I_1 = \lambda_1^2 + \lambda_2^2 - 2, \quad I_2 = \lambda_1^2 \lambda_2^2 - 1. \quad (5)$$

Barthès-Biesel *et al.* [44] showed that for  $C_a \gtrsim 10.0$ , the tension of a Skalak membrane becomes nearly independent of  $C_a$  under a simple uniaxial deformation, so  $C_a$  is set to 10.0 for all of the simulations in the present work. This model predicts a strain hardening behavior of the membrane, consistent with the experimentally determined response of an RBC membrane to stretching [10, 45]. The deformability of the capsule is characterized by the nondimensional capillary number  $\text{Ca} = \eta \dot{\gamma} c / G$ , where  $c$  is the half-length of the prolate capsule. In this work the capsules are taken to be stiff in accordance with the biomechanical properties of the membrane of a sickle RBC, with  $\text{Ca}$  lower than 0.2 assuming the shear rate  $\dot{\gamma}$  of blood flow in the microcirculation  $\sim 10 - 10^3 \text{ s}^{-1}$  [46], the characteristic length  $c$  of a

typical sickle RBC  $\sim 5 - 6 \mu\text{m}$  [12], the viscosity of plasma  $\eta \sim 1.71 \text{ mPa s}$  [47], and the in-plane shear modulus of a sickle RBC membrane  $G \sim 29.8 \mu\text{N/m}$  [12]. The bending modulus of the capsule  $K_B$  is expressed nondimensionally by  $\hat{\kappa}_B = K_B / c^2 G$ , which is  $\mathcal{O}(10^{-4} - 10^{-2})$  in the physiological context [48, 49]; here we set  $\hat{\kappa}_B = 0.04$  for all capsules. In this work, the natural shape for shear and the spontaneous shape for bending elasticities of the capsule membrane are both chosen to be the same as its rest shape, so that any in-plane or out-of-plane deformation would lead to an increase in the membrane energy and thus to an elastic restoring force. The total membrane strain force density  $\mathbf{f}^m$  can be obtained by taking the first variation of the total membrane energy  $E$ , which then gives:

$$\mathbf{f}^m = \mathbf{f}^b + \mathbf{f}^s, \quad (6)$$

where  $\mathbf{f}^b$  and  $\mathbf{f}^s$  are bending and shear elastic force densities, respectively. The capsule membrane is discretized into 320 piecewise flat triangular elements, resulting in 162 nodes. We have verified that increasing the number of nodes makes no difference to the cell dynamics. Based on this discretization, the calculation of the total membrane force density  $\mathbf{f}^m$  follows the work of Kumar and Graham [50] and Sinha and Graham [10] using approaches given by Charrier *et al.* [51] for the in-plane shear force density  $\mathbf{f}^s$  and Meyer *et al.* [52] for the out-of-plane bending force density  $\mathbf{f}^b$ , respectively. Details regarding these calculations are found in [50] and [10].

## B. Fluid motion

As noted in Section II A, the characteristic shear rate  $\dot{\gamma}$  of blood flow in the microcirculation is  $\sim 10 - 10^3 \text{ s}^{-1}$  [46], the length scale  $c$  of a typical sickle RBC  $\sim 5 - 6 \mu\text{m}$  [12], the viscosity of plasma  $\eta \sim 1.71 \text{ mPa s}$  [47], and its density  $\rho \sim 10^3 \text{ kg/m}^3$ . The magnitude of the particle Reynolds number  $\text{Re}_p = \rho \dot{\gamma} c^2 / \eta$  obtained using these parameters is  $\sim \mathcal{O}(10^{-4} - 10^{-2})$ , which is assumed to be sufficiently small so that the fluid motion is governed by the Stokes equation. To determine the velocity field at each time instant, we employ a boundary integral method [50, 53] for simulation in unbounded simple shear flow. The fluid velocity  $\mathbf{u}$  at any point  $\mathbf{x}_0$  in the unbounded domain can be written as:

$$u_j(\mathbf{x}_0) = u_j^\infty(\mathbf{x}_0) + \int_S q_i(\mathbf{x}) G_{ji}(\mathbf{x}_0, \mathbf{x}) dS(\mathbf{x}), \quad (7)$$

where  $\mathbf{q}(\mathbf{x}_0)$  is a single-layer density that satisfies

$$q_j(\mathbf{x}_0) + \frac{\lambda - 1}{4\pi(\lambda + 1)} n_k(\mathbf{x}_0) \int_S q_i(\mathbf{x}) T_{jik}(\mathbf{x}_0, \mathbf{x}) dS(\mathbf{x}) = -\frac{1}{4\pi\mu} \left( \frac{\Delta f_j(\mathbf{x}_0)}{\lambda + 1} + \frac{\lambda - 1}{\lambda + 1} f_j^\infty(\mathbf{x}_0) \right). \quad (8)$$

Here  $\mathbf{u}^\infty(\mathbf{x}_0)$  is the undisturbed fluid velocity at a given point  $\mathbf{x}_0$ ,  $S$  denotes the surface of the particle;  $\mathbf{f}^\infty(\mathbf{x}_0)$  is the traction at a given point due to the stress generated in the fluid corresponding to the undisturbed flow  $\mathbf{u}^\infty(\mathbf{x}_0)$ ;  $\mathbf{f}(\mathbf{x})$  is the hydrodynamic traction jump

across the membrane interface, which relates to the total membrane force density by  $\mathbf{f}(\mathbf{x}) = -\mathbf{f}^m$  assuming the membrane equilibrium condition;  $\mathbf{G}$  and  $\mathbf{T}$  are the Green's function and its associated stress tensor for Stokes flow in an unbounded domain. Details of the numerical method are described in [50] Once the flow field is determined, the positions of the element nodes on the discretized capsule membrane are advanced using a second-order Adams-Bashforth method with time step  $\Delta t = 0.02Ca l$ , where  $l$  is the minimum node-to-node distance.

### C. Model validation

The implementation of the numerical methods used in this work has been validated with test problems on the velocity of rigid particles and drops between parallel walls in pressure driven flow, and the numerical algorithms for the capsule membrane mechanics including in-plane shear elasticity and out-of-plane bending elasticity have been validated with the deformation of spherical capsules in simple shear flow. For details, see [50] and [10]. As a further validation, we compare here the numerically determined inclination profile for a stiff prolate spheroid ( $Ca = 0.06$ ) with the prediction by Jeffery's theory [24],

$$\tan \phi = r_p \tan \left( \frac{\dot{\gamma} t}{r_p + r_p^{-1}} + \phi_0 \right), \quad (9)$$

where  $\phi$  is the inclination angle between the major axis of the prolate spheroid ( $\mathbf{p}$ ) and the  $y$  direction, and  $\phi_0$  its initial value; here  $\phi_0 = \pi/2$  since the prolate spheroid is initially aligned with the  $x$  axis. FIG. 2 shows the evolution of  $\phi$  with nondimensionalized time  $\dot{\gamma} t$ . Good agreement between numerical simulation and Jeffery's theory (Eq. 9) is observed for the prolate spheroid with either a low ( $r_p = 2.0$ ) or a high ( $r_p = 4.8$ ) aspect ratio. The very small discrepancy in each case derives from the non-zero deformability of the prolate spheroid, and vanishes as  $Ca$  approaches zero.

## III. RESULTS AND DISCUSSION

### A. Dynamics of deformable straight prolate capsules

In this section, we investigate the dynamics of a stiff prolate spheroidal capsule ( $r_p = 4.8$ ,  $Ca = 0.12$ ). Here we keep the viscosity ratio  $\gamma = 1$ . We first consider the case where the prolate capsule is initially aligned with the  $x$  axis, *i.e.*,  $\alpha = 0$ . The long-time trajectories (up to  $\dot{\gamma} t = 2000$ ) of the end-to-end vector  $\mathbf{p}$  and the normal vector  $\mathbf{n}$  on the unit sphere are plotted in FIG. 3. In this case, both  $\mathbf{p}$  and  $\mathbf{n}$  appear to trace out a closed circle, indicating that the capsule is taking a steady symmetric tumbling motion in the  $x$ - $y$  plane.

We then consider a perturbation of the initial orientation by a small angle  $\alpha = \pi/36$ . The trajectories of  $\mathbf{p}$  and  $\mathbf{n}$  vectors on the unit sphere are shown in FIG. 4. It can be observed that both  $p_z$  and  $n_z$  show an oscillation around zero whose amplitude decays to zero as time increases (FIG. 5), where  $p_z$  and  $n_z$  are the components of  $\mathbf{p}$  and  $\mathbf{n}$  in the vorticity direction, respectively. The director  $\mathbf{p}$  crosses the  $x$ - $y$  plane back-and-forth (as indicated by the sign change of  $p_z$  in FIG. 5), exhibiting non-Jeffery-like dynamics, in the sense that for Jeffery orbits, the director  $\mathbf{p}$  never crosses the shear-gradient plane. The dynamics of  $\mathbf{n}$  are much

more complicated. The trajectory reaches a quasisteady state position on either hemisphere alternately every time  $p_z$  changes its sign, as observed in FIG. 4(d), and the quasisteady state position gets closer and closer to zero, which is consistent with the damped oscillation of  $n_z$  (FIG. 5). All these behaviors indicate that under small perturbation, the orbit of a slightly deformable prolate spheroidal capsule evolves back towards the symmetric tumbling motion in the  $x$ - $y$  plane, indicating that the symmetric tumbling orbit in the  $x$ - $y$  plane is stable.

By further increasing the initial angle  $\alpha$  of the prolate spheroid off the  $x$  axis, we observe that for an arbitrary  $\alpha$ , the orbit of the prolate spheroid evolves towards the symmetric tumbling in the  $x$ - $y$  plane regardless of the initial orientation. This shows that the in-plane symmetric tumbling is the globally stable state for the prolate spheroidal capsules in the parameter regime considered. This result is similar to that by Villone *et al.* [36] for a neo-Hookean elastic solid prolate spheroid: when initially oriented off the shear plane, a stiff particle with a high aspect ratio would evolve towards tumbling motion in the shear plane with  $p_z$  approaching zero. In addition, this stable in-plane tumbling orbit that we find for an inertialess slender prolate capsule was also observed in the analytical prediction by Subramanian and Koch [28] and the numerical investigation by Mao and Alexeev [29] for a solid prolate particle considering particle inertia, except that in our work the degeneracy of Jeffery's solution [24] due to the linearity of the Stokes flow is broken by deformability of the capsule instead of inertial effect.

Prior to our work, Dupont *et al.* and Cordasco and Bagchi [32, 33] both investigated the out-of-shear plane dynamics of isolated prolate capsules in simple shear flow, revealing that a prolate capsule takes rolling, or a drifting precession towards the vorticity axis, as the stable dynamical mode at lower capillary numbers, which is different from our result. In our work, the spontaneous shape used for modeling the bending resistance of the membrane is chosen to be the same as the rest shape of the prolate capsule, while in Cordasco and Bagchi [33] the spontaneous curvature was set to zero everywhere for the membrane surface, *i.e.* the spontaneous shape was a flat sheet; in Dupont *et al.* [32], bending resistance was not even incorporated into the membrane mechanics. In addition, both Dupont *et al.* [32] and Cordasco and Bagchi [33] used a much lower value for the area dilatation parameter  $C_a$  in the Skalak membrane model [34], *i.e.*,  $C_a = 1.0$ , while we set  $C_a$  to 10.0 which allows less area change of the membrane; they focused on prolate capsules with much lower asphericity ( $r_p = 3.0$ ) as compared to the more elongated prolate capsule ( $r_p = 4.8$ ) in our study. We have been able to reproduce Cordasco and Bagchi's result [33] for a prolate capsule at  $Ca = 0.2$  with the spontaneous curvature, aspect ratio, and membrane area dilatation parameter of the capsule tuned to the same corresponding values as used in their work, which demonstrates that the difference in the stable orbits originates from the differences in model as described above, with an indication that the capsule dynamics may be sensitive to its spontaneous shape.

## B. Dynamics of deformable curved prolate capsules

In this section, we perform a systematic investigation of the dynamics of curved prolate spheroids at low  $Ca$  as described in Section II A. The results for  $\lambda = 1$  are presented and discussed first.

We first examine the early-stage dynamics ( $0 < \dot{\gamma}t \lesssim 500$ ) of curved prolate capsules in the case of  $Ca = 0.12$  and  $K = 0.36$  with various initial orientations, beginning with the case where  $\mathbf{p}$  is initially aligned with the  $x$  direction and  $\mathbf{n}$  with the  $z$  direction. Here the trajectory of  $\mathbf{p}$  traces out a closed circle on the unit sphere (FIG. 6(a)), while  $\mathbf{n}$  remains fixed (FIG. 6(b)), which indicates that the capsule is taking a sideways Jeffery-like tumbling motion. In the case of  $[\alpha, \beta] = [0, \pi/6]$  (FIG. 7(a) and 7(d)),  $\mathbf{p}$  is observed to cross the  $x$ - $y$  plane back and forth, exhibiting a wobbling motion which is not Jeffery-like, as shown in FIG. 8(a). We then consider the case where  $[\alpha, \beta] = [0, \pi/2]$ , *i.e.*, the capsule is completely lying in the  $x$ - $y$  plane initially, with  $\mathbf{p}$  aligned with the  $x$  direction and  $\mathbf{n}$  with the  $y$  direction. The closed circular orbits on the unit sphere indicate that the capsule is taking a rigid-body-like symmetric tumbling motion as its early-stage dynamics (FIG. 7(b) and 7(e)). In the case  $[\alpha, \beta] = [\pi/6, \pi/3]$ , a more Jeffery-like orbit is observed (FIG. 7(c) and 7(f)), in the sense that  $\mathbf{p}$  does not cross the shear plane. Here it is noteworthy that in a Jeffery-like orbit, the trajectory of  $\mathbf{n}$  spans both hemispheres divided by the shear plane on the unit sphere (FIG. 7(f)), while it only appears on one hemisphere of the unit sphere in the non-Jeffery-like orbit observed in the case of  $[\alpha, \beta] = [0, \pi/6]$  described above (FIG. 7(d)).

The early-stage dynamics of the curved prolate capsules described above, however, are all found to be long-lived transients. FIG. 9 shows the long-time ( $\dot{\gamma}t > 1000$ ) trajectories of the  $\mathbf{p}$  vector of curved prolate capsules with different initial orientations on the unit sphere. The long-time dynamics of the capsules, regardless of their early-stage orbits, all evolve into a quasiperiodic kayaking motion that might be described as a “modulated Jeffery orbit”. We will elaborate below on the connection to Jeffery orbit, but for the moment we simply note that the long-time motion of  $\mathbf{p}$  is independent of the initial orientation of the capsules, as indicated by the nearly identical trajectories of  $\mathbf{p}$  on the unit sphere (FIG. 9). Qualitatively, these orbits have a fast time scale corresponding to one cycle of kayaking, with a much longer time scale describing a slow modulation of the orbit. Each kayaking cycle is slightly different than the previous, a fact that can be attributed to the dynamics of  $\mathbf{n}$ , which are coupled to those of  $\mathbf{p}$  for a curved particle (or indeed any nonaxisymmetric particle). FIG. 8(b) shows snapshots of a long-time orbit. Recall that quasiperiodic orbits are also found for triaxial ellipsoids [26] and curved rigid fibers [37]. In all case this is associated with the breaking of axisymmetry and the coupling between  $\mathbf{p}$  and  $\mathbf{n}$ . We do not observe chaotic dynamics under any conditions considered here.

The two time scales noted above are also observed in the long-time center-of-mass position profiles shown in FIG. 10, with a shorter time scale representing one cycle of the kayaking motion described above superimposed onto a longer time scale corresponding to the orbit modulation. In the parameter regime considered here, we have seen no evidence of drift in the  $y$  (“wall normal”) direction. This is in contrast to the observations of [37] for curved rigid fibers in the “flipping and scooping” regime; we believe the difference arises from the modest aspect ratios considered here, which are much smaller than those studied by [37]. We do, however, observe a transient phase of spanwise drift in the case of the capsule initialized to perform a sideways tumbling motion. This vanishes once the cell reaches its long-time orientational trajectory. Although there is no drift at long times, both the  $y$  and  $z$  components of the center of mass oscillate as the cell kayaks.

Now we return to the issue of the connection with Jeffery orbits. The blue curve in Figure 11(a) shows the long-time trajectory for the case  $Ca = 0.12$ ,  $K = 0.36$  (for which FIG. 9 shows the trajectory of  $\mathbf{p}$  on the unit sphere), expressed in spherical coordinates  $\phi$  and  $\theta$  based on the coordinate system used in Jeffery's theory [24], *i.e.*,  $\phi$  is the azimuthal angle with respect to the  $y$  axis and  $\theta$  is the polar angle with respect to the  $z$  axis. With this representation, we can find a mean trajectory  $\bar{\theta}(\phi)$  by averaging  $\theta$  over the trajectory at each  $\phi$ . This result is represented by the black circles in FIG. 11(a). For a true Jeffery orbit of a rigid spheroid with orbit constant  $C$  and aspect ratio  $\ell$  the relation between  $\phi$  and  $\theta$  is given by

$$\tan \theta = \frac{C\ell}{(\ell^2 \cos^2 \phi + \sin^2 \phi)^{1/2}}. \quad (10)$$

We have found that in all cases considered here, we can approximate, with very good accuracy, the curve  $\bar{\theta}(\phi)$  as a Jeffery orbit for a spheroid with an effective orbit constant  $C_{\text{eff}}$  and effective aspect ratio  $\ell_{\text{eff}}$ . That is, we can use  $C_{\text{eff}}$  and  $\ell_{\text{eff}}$  as fitting parameters in the expression

$$\tan \bar{\theta} = \frac{C_{\text{eff}}\ell_{\text{eff}}}{(\ell_{\text{eff}}^2 \cos^2 \phi + \sin^2 \phi)^{1/2}}. \quad (11)$$

The red curve in FIG. 11(a) shows this approximation for  $Ca = 0.12$ ,  $K = 0.36$ .

This observation enables us to succinctly characterize the effects of deformability and curvature on the long-time dynamics. We have computed long-time trajectories over a range of  $Ca$  and  $K$  and computed the resulting values of  $C_{\text{eff}}$  and  $\ell_{\text{eff}}$ . These results are summarized in FIG. 12. It is observed that  $\ell_{\text{eff}}$  increases weakly as  $K$  increases but shows very little dependency on  $Ca$  (FIG. 12(b)). More importantly,  $C_{\text{eff}}$  decreases as either  $Ca$  or  $K$  increases (FIG. 12(a)), indicating a shift of the orbit towards log-rolling motion as curvature or deformability increase.

For completeness, we briefly consider the deviations of the instantaneous trajectories from the mean curve  $\bar{\theta}(\phi)$ . The maximum positive and negative deviations from the mean when  $\phi = \pi$  are denoted as  $\theta^+$  and  $\theta^-$  (FIG. 11(a)). The relative deviations  $\Delta\theta / \bar{\theta}$  are found to be insensitive to the parameters in the range considered here, with  $0.16 < \Delta\theta^+ / \bar{\theta} < 0.19$ , and  $-0.35 < \Delta\theta^- / \bar{\theta} < -0.30$ .

Under physiological conditions, the cytoplasmic fluid inside an RBC has a higher viscosity than the surrounding plasma [12];  $\lambda \approx 5$ . We have therefore also performed simulations with  $\lambda = 5$ , finding that the long-time trajectory of a curved prolate capsule within the parameter space considered in this work still indicates a quasiperiodic kayaking motion with no net cross-stream drift, similar to what is observed for  $\lambda = 1$ . Furthermore, the  $\bar{\theta}(\phi)$  can still be well approximated using Jeffery's analytical solution (Eq. 11), with  $C_{\text{eff}}$  and  $\ell_{\text{eff}}$  determined by fitting. FIG. 11(b) shows an example of this fit, with  $Ca = 0.06$ ,  $K = 0.39$ ,  $\lambda = 5$ . FIG. 12

shows the values of  $C_{\text{eff}}$  and  $\ell_{\text{ff}}$  for  $\lambda = 5$  over the same range of  $Ca$  and  $K$  considered for  $\lambda = 1$ . The values of either parameter only show minor differences between the two viscosity ratios, so the trends with  $Ca$  and  $K$  for  $\lambda = 1$  still hold qualitatively for  $\lambda = 5$ .

#### IV. CONCLUSION

We investigated the dynamics of neutrally-buoyant, slightly deformable straight and curved prolate capsules subjected to unbounded simple shear flow at zero Reynolds number using direct simulations. The curved prolate capsules in this work serve as a model for the typical crescent-shaped sickle RBCs in sickle cell disease (SCD), and we aimed to show the effects of initial orientation, membrane deformability and curvature of the capsules on their dynamics.

The dynamics of the capsules are simulated using a full model incorporating both shear and bending elasticities. The parameter regime is based on the range of experimentally determined values for blood flow in the microcirculation. We revealed that with low deformability, straight prolate spheroidal capsules take tumbling in the shear plane as the unique globally stable orbit independent of the initial orientation. As the trajectories of the straight prolate capsules transiently evolve towards this in-plane tumbling, the director can cross the  $x$ - $y$  plane back and forth, showing a non-Jeffery-like motion.

Curved prolate capsules exhibit complicated and interesting dynamics due to the combined effects of membrane deformability  $Ca$  and the curvature  $K$  of the capsules. At short times, a non-Jeffery-like behavior, in which the director (end-to-end vector) of the capsule crosses the shear-gradient plane periodically, is observed for specific initial orientations. Steady drift of the center of mass in the vorticity direction is also observed for some initial orientations. At long times, however, the trajectories of the curved capsules, regardless of their initial orientations, all evolve towards a Jeffery-like quasiperiodic kayaking orbit with the center-of-mass position of a curved capsule crossing the shear plane periodically instead of remaining in it. No cross-stream drift is found. Under all conditions studied, the average of the long-time orbit can be well approximated using the analytical solution for Jeffery orbits with an effective orbit constant  $C_{\text{eff}}$  and aspect ratio  $\ell_{\text{ff}}$ . A parameter study further reveals that  $C_{\text{eff}}$  decreases as the capsule becomes more deformable or curved, indicating a shift of the orbit towards log-rolling motion. This conclusion holds qualitatively as the viscosity ratio between the fluids inside and outside the capsule increases from  $\lambda = 1$  to  $\lambda = 5$ .

Overall, these results represent an effort to understand the motion of single sickle RBCs, taking into account the pathologically altered shape as well as the elastic and bending moduli of these diseased cells. Major aspects of the pathophysiology of SCD remain poorly understood and currently, there is an increased focus on how aberrant cell interactions, between sickle RBCs and other blood cells (*i.e.* platelets and leukocytes) or between sickle RBCs and endothelial cells, may contribute to phenomena such as thrombosis or vascular inflammation that are known to be vital part of the process of SCD. In particular, the effective orbit constant of a sickle cell moving near a blood vessel wall may reflect the propensity for that cell to collide with and potentially damage the wall. For example, a sickle cell with a high orbit constant tends to tumbling or kayaking motion, which physically will

have a greater chance to poke and damage the vessel wall than a rolling cell with a much lower orbit constant. In addition, the comparison of our results with those by Cordasco and Bagchi [33] with different membrane mechanics suggests that the dynamics of the capsules have a nontrivial dependence on the membrane behavior. Future work, both computational and experimental, will need to address how best to model this behavior for sickle cells in order to reflect the dynamical motions of sickle cells in blood flow. More broadly, the results of this work demonstrate how the mechanical properties and distorted cell shape of sickle RBCs lead to distinct trajectories that may, in turn, cause pathologic biophysical activation of other cells, and may provide insight into how these disparate aspects of SCD are ultimately linked. That knowledge will then lead to improved methods to diagnose complications of and new therapeutic targets for SCD.

## ACKNOWLEDGMENTS

This work was supported by NSF Grant No. CBET-1436082 and NIH Grant No. R21MD011590-01A1

## References

- [1]. Mohandas N and Evans E, "Mechanical properties of the red cell membrane in relation to molecular structure and genetic defects," *Annu. Rev. Biophys. Biomol. Struct* 23, 787–818 (1994). [PubMed: 7919799]
- [2]. Goldsmith HL, Marlow J, and MacIntosh FC, "Flow behaviour of erythrocytes. I. Rotation and deformation in dilute suspensions," *Proc. R. Soc. Lond., B, Biol. Sci* 182, 351–384 (1972).
- [3]. Fischer TM, Stohr-Lissen M, and Schmid-Schonbein H, "The red cell as a fluid droplet: tank tread-like motion of the human erythrocyte membrane in shear flow," *Science* 202, 894–896 (1978). [PubMed: 715448]
- [4]. Abkarian M, Faivre M, and Viallat A, "Swinging of red blood cells under shear flow," *Phys. Rev. Lett* 98, 188302 (2007). [PubMed: 17501614]
- [5]. Skotheim JM and Secomb TW, "Red blood cells and other nonspherical capsules in shear flow: Oscillatory dynamics and the tank-treading-to-tumbling transition," *Phys. Rev. Lett* 98, 078301 (2007). [PubMed: 17359066]
- [6]. Dupire J, Abkarian M, and Viallat A, "Chaotic dynamics of red blood cells in a sinusoidal flow," *Phys. Rev. Lett* 104, 168101 (2010). [PubMed: 20482082]
- [7]. Fedosov DA, Caswell B, and Karniadakis GE, "A multiscale red blood cell model with accurate mechanics, rheology, and dynamics," *Biophys. J* 98, 2215–2225 (2010). [PubMed: 20483330]
- [8]. Fedosov DA, Lei H, Caswell B, Suresh S, and Karniadakis GE, "Multiscale modeling of red blood cell mechanics and blood flow in malaria," *PLoS Comp. Biol* 7, e1002270 (2011).
- [9]. Yazdani AZK and Bagchi P, "Phase diagram and breathing dynamics of a single red blood cell and a biconcave capsule in dilute shear flow," *Phys. Rev. E* 84, 026314 (2011).
- [10]. Sinha K and Graham MD, "Dynamics of a single red blood cell in simple shear flow," *Phys. Rev. E* 92, 042710 (2015).
- [11]. Minetti C, Audemar V, Podgorski T, and Couplier G, "Dynamics of a large population of red blood cells under shear flow," *J. Fluid Mech* 864, 408–448 (2019).
- [12]. Byun H, Hillman TR, Higgins JM, Diez-Silva M, Peng Z, Dao M, Dasari RR, Suresh S, and Park Y, "Optical measurement of biomechanical properties of individual erythrocytes from a sickle cell patient," *Acta Biomater.* 8, 4130–4138 (2012). [PubMed: 22820310]
- [13]. Lei H and Karniadakis GE, "Predicting the morphology of sickle red blood cells using coarse-grained models of intracellular aligned hemoglobin polymers," *Soft Matter* 8, 4507–4516 (2012).
- [14]. Dou Q and Ferrone FA, "Simulated formation of polymer domains in sickle hemoglobin," *Biophys. J* 65, 2068–2077 (1993). [PubMed: 8298036]

- [15]. Li X, Caswell B, and Karniadakis GE, “Effect of chain chirality on the self-assembly of sickle hemoglobin,” *Biophys. J.* 103, 1130–1140 (2012). [PubMed: 22995485]
- [16]. Lu L, Li X, Vekilov PG, and Karniadakis GE, “Probing the twisted structure of sickle hemoglobin fibers via particle simulations,” *Biophys. J.* 110, 2085–2093 (2016). [PubMed: 27166816]
- [17]. Papageorgiou DP, Abidi SZ, Chang H, Li X, Kato GJ, Karniadakis GE, Suresh S, and Dao M, “Simultaneous polymerization and adhesion under hypoxia in sickle cell disease,” *Proc. Natl. Acad. Sci. USA* 115, 9473–9478 (2018). [PubMed: 30190429]
- [18]. Xu M, Papageorgiou DP, Abidi SZ, Dao M, Zhao H, and Karniadakis GE, “A deep convolutional neural network for classification of red blood cells in sickle cell anemia,” *PLoS Comp. Bio* 13, 1–27 (2017).
- [19]. Messer MJ and Harris JW, “Filtration characteristics of sickle cells: Rates of alteration of filterability after deoxygenation and reoxygenation, and correlations with sickling and unsickling,” *J. Lab. Clin. Med* 76, 537–547 (1970). [PubMed: 5458019]
- [20]. Nash GB, Johnson CS, and Meiselman HJ, “Mechanical properties of oxygenated red blood cells in sickle cell (HbSS) disease,” *Blood* 63, 73–82 (1984). [PubMed: 6689955]
- [21]. Evans EA and Mohandas N, “Membrane-associated sickle hemoglobin: a major determinant of sickle erythrocyte rigidity,” *Blood* 70, 1443–1449 (1987). [PubMed: 3663941]
- [22]. Li X, Dao M, Lykotrafitis G, and Karniadakis GE, “Biomechanics and biorheology of red blood cells in sickle cell anemia,” *J. Biomech* 50, 34–41 (2017). [PubMed: 27876368]
- [23]. Bertles JF and Döbler J, “Reversible and irreversible sickling: a distinction by electron microscopy,” *Blood* 33, 884–898 (1969). [PubMed: 5795766]
- [24]. Jeffery GB, “The motion of ellipsoidal particles immersed in a viscous fluid,” *Proc. Roy. Soc. Lond. A* 102, 161–179 (1922).
- [25]. Bretherton FP, “The motion of rigid particles in a shear flow at low Reynolds number,” *J. Fluid Mech* 14, 284–304 (1962).
- [26]. Hinch EJ and Leal LG, “Rotation of small non-axisymmetric particles in a simple shear flow,” *J. Fluid Mech* 92, 591–607 (1979).
- [27]. Yarin AL, Gottlieb O, and Roisman IV, “Chaotic rotation of triaxial ellipsoids in simple shear flow,” *J. Fluid Mech* 340, 83–100 (1997).
- [28]. Subramanian G and Koch DL, “Inertial effects on the orientation of nearly spherical particles in simple shear flow,” *J. Fluid Mech* 557, 257–296 (2006).
- [29]. Mao W and Alexeev A, “Motion of spheroid particles in shear flow with inertia,” *J. Fluid Mech* 749, 145–166 (2014).
- [30]. Walter J, Salsac A, and Barthès-Biesel D, “Ellipsoidal capsules in simple shear flow: prolate versus oblate initial shapes,” *J. Fluid Mech* 676, 318–347 (2011).
- [31]. Luo Z and Bai B, “Dynamics of nonspherical compound capsules in simple shear flow,” *Phys. Fluids* 28, 101901 (2016).
- [32]. Dupont C, Salsac A, and Barthès-Biesel D, “Off-plane motion of a prolate capsule in shear flow,” *J. Fluid Mech* 721, 180–198 (2013).
- [33]. Cordasco D and Bagchi P, “Orbital drift of capsules and red blood cells in shear flow,” *Phys. Fluids* 25, 091902 (2013).
- [34]. Skalak R, Tozeren A, Zarda RP, and Chien S, “Strain energy function of red blood-cell membranes,” *Biophys. J.* 13, 245–280 (1973). [PubMed: 4697236]
- [35]. Gao T, Hu HH, and Castañeda PP, “Shape dynamics and rheology of soft elastic particles in a shear flow,” *Phys. Rev. Lett* 108, 058302 (2012). [PubMed: 22400968]
- [36]. Villone MM, D’Avino G, Hulsken MA, and Maffettone PL, “Dynamics of prolate spheroidal elastic particles in confined shear flow,” *Phys. Rev. E* 92, 062303 (2015).
- [37]. Wang J, Tozzi EJ, Graham MD, and Klingenberg DJ, “Flipping, scooping, and spinning: Drift of rigid curved nonchiral fibers in simple shear flow,” *Phys. Fluids* 24, 123304 (2012).
- [38]. Crowdy D, “Flipping and scooping of curved 2D rigid fibers in simple shear: The Jeffery equations,” *Phys. Fluids* 28, 053105 (2016).

- [39]. Lei H and Karniadakis GE, “Probing vasoocclusion phenomena in sickle cell anemia via mesoscopic simulations,” *Proc. Natl. Acad. Sci. USA* 110, 11326–11330 (2013). [PubMed: 23798393]
- [40]. Lei H and Karniadakis GE, “Multiscale modeling of sickle cell anemia,” in *Modeling the Heart and the Circulatory System* (Springer International Publishing, 2015) pp. 119–156.
- [41]. Deng Y, Papageorgiou DP, Chang H, Abidi SZ, Li X, Dao M, and Karniadakis GE, “Quantifying shear-induced deformation and detachment of individual adherent sickle red blood cells,” *Biophys. J* 116, 360–371 (2019). [PubMed: 30612714]
- [42]. Canham PB, “The minimum energy of bending as a possible explanation of the biconcave shape of the human red blood cell,” *J. Theor. Biol* 26, 61–81 (1970). [PubMed: 5411112]
- [43]. Helfrich W, “Elastic properties of lipid bilayers: theory and possible experiments,” *Z. Naturforsch C* 28, 693–703 (1973). [PubMed: 4273690]
- [44]. Barthès-Biesel D, Diaz A, and Dhenin E, “Effect of constitutive laws for two-dimensional membranes on flow-induced capsule deformation,” *J. Fluid Mech* 460, 211–222 (2002).
- [45]. Mills JP, Qie L, Dao M, Lim CT, and Suresh S, “Nonlinear elastic and viscoelastic deformation of the human red blood cell with optical tweezers,” *Mech. Chem. Biosyst* 1, 169–180 (2004). [PubMed: 16783930]
- [46]. Lipowsky HH, “In vivo studies of blood rheology in the microcirculation in an in vitro world: Past, present and future,” *Biorheology* 50, 3–16 (2013). [PubMed: 23619149]
- [47]. Laogun AA, Ajayi NO, Osamo NO, and Okafor LA, “Plasma viscosity in sickle-cell anaemia,” *Clin. Phys. Physiol. Meas* 1, 145 (1980).
- [48]. Evans J, Gratzler W, Mohandas N, Parker K, and Sleep J, “Fluctuations of the red blood cell membrane: relation to mechanical properties and lack of ATP dependence,” *Biophys. J* 94, 4134–4144 (2008). [PubMed: 18234829]
- [49]. Betz T, Lenz M, Joanny J, and Sykes C, “ATP-dependent mechanics of red blood cells,” *Proc. Natl. Acad. Sci. USA* 106, 15320–15325 (2009). [PubMed: 19717437]
- [50]. Kumar A and Graham MD, “Accelerated boundary integral method for multiphase flow in non-periodic geometries,” *J. Comput. Phys* 231, 6682–6713 (2012).
- [51]. Charrier JM, Shrivastava S, and Wu R, “Free and constrained inflation of elastic membranes in relation to thermoforming – non-axisymmetric problems,” *J. Strain Anal. Eng. Des* 24, 55–74 (1989).
- [52]. Meyer M, Desbrun M, Schroeder P, and Barr AH, “Discrete differential geometry operators for triangulated 2-manifolds,” *Visualization and Mathematics* 3, 34–57 (2002).
- [53]. Pozrikidis C, *Boundary integral and singularity methods for linearized viscous flow*, Cambridge Texts in Applied Mathematics (Cambridge University Press, 1992).

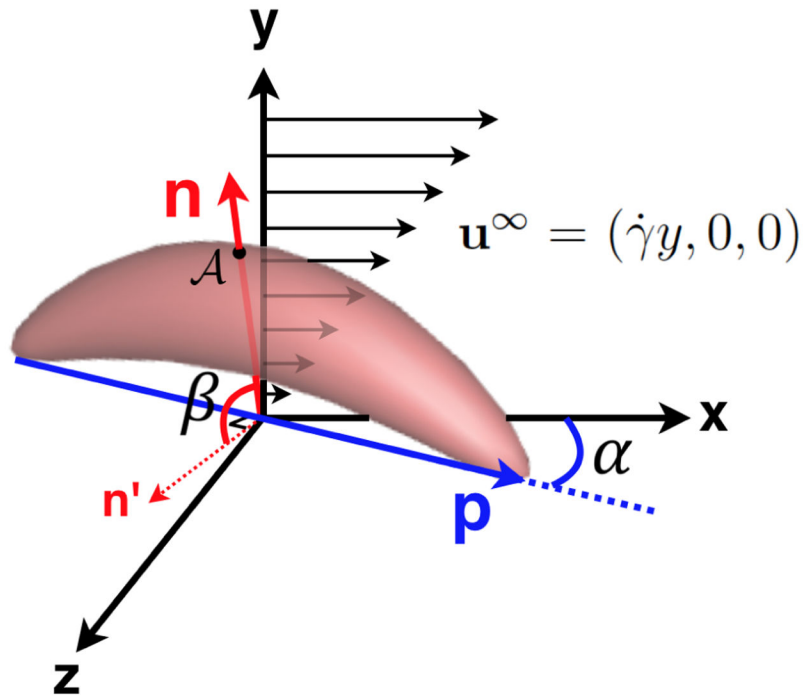


**FIG. 1:**  
Schematic of the initial orientation of a curved prolate capsule in unbounded simple shear flow.

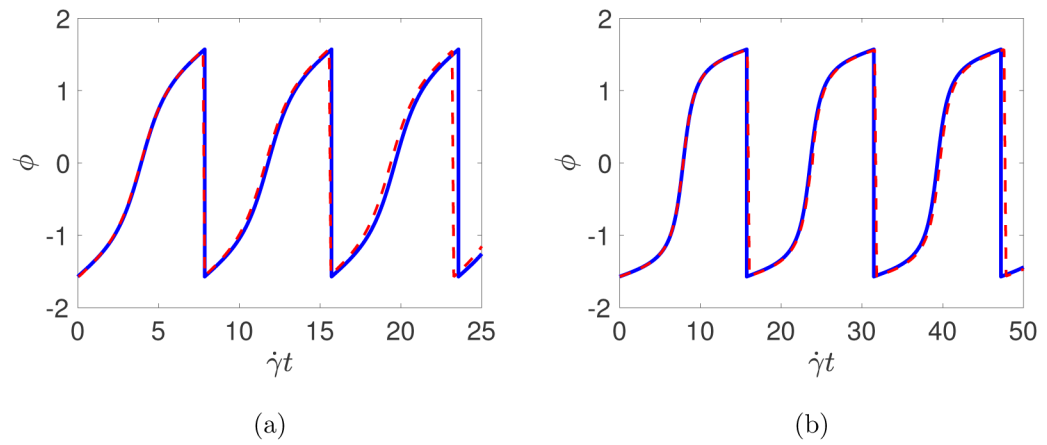


**FIG. 2:** Evolution of inclination angle  $\phi$  for a stiff prolate spheroid ( $Ca = 0.06$ ) with (a)  $r_p = 2.0$  and (b)  $r_p = 4.8$ , respectively. Solid blue lines are predictions by Jeffery's theory and red dashed lines are simulation results.

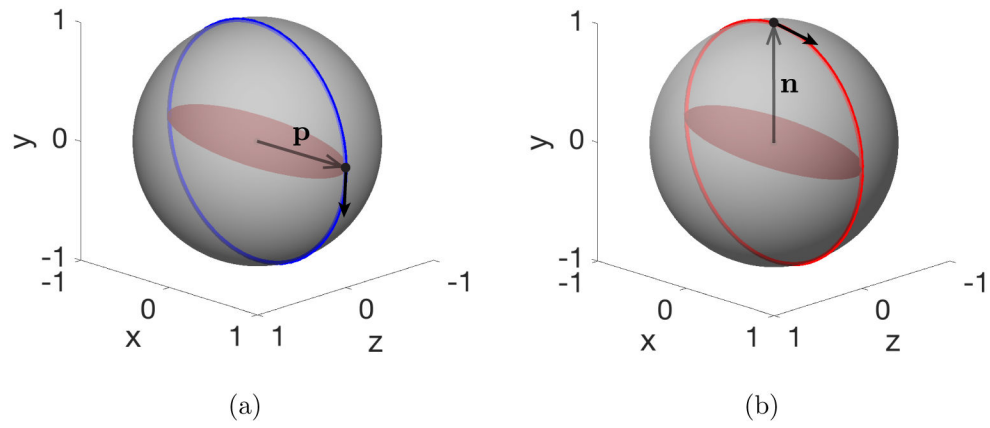


**FIG. 3:** Trajectories on the unit sphere of (a)  $\mathbf{p}$  and (b)  $\mathbf{n}$  for a prolate spheroid ( $r_p = 4.8$ ,  $\text{Ca} = 0.12$ ) with initial orientation  $\alpha = 0$  (up to  $\dot{\gamma}t = 2000$ ).

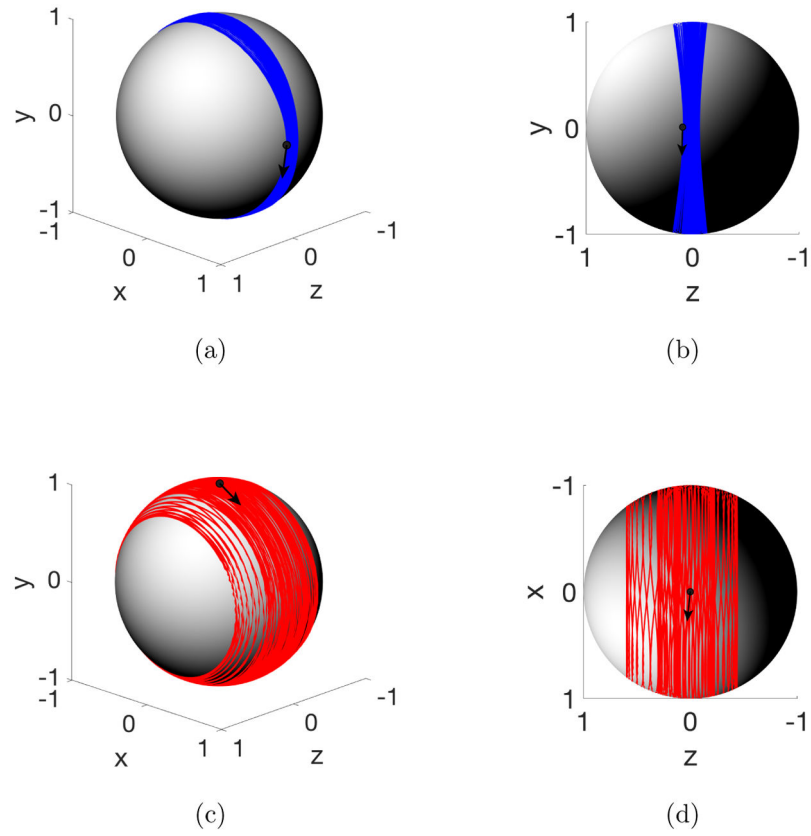


**FIG. 4:** Trajectories on the unit sphere of  $\mathbf{p}$  ((a) and (b) ( $y$ - $z$  view)) and  $\mathbf{n}$  ((c) and (d) ( $x$ - $z$  view)) for a prolate spheroid ( $r_p = 4.8$ ,  $Ca = 0.12$ ) with initial orientation  $\alpha = \pi/36$ .

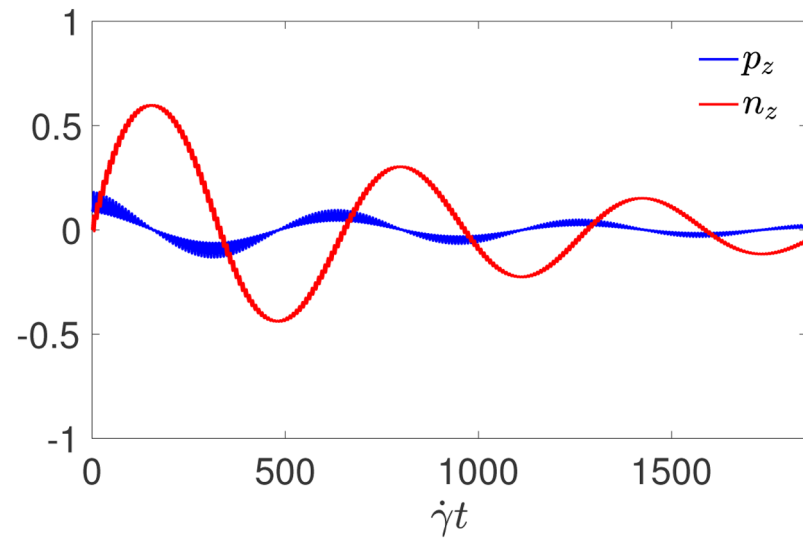


**FIG. 5:** The evolution of the  $p_z$  and  $n_z$  for a prolate spheroid ( $r_p = 4.8$ ,  $Ca = 0.12$ ) with initial orientation  $\alpha = \pi/36$ .

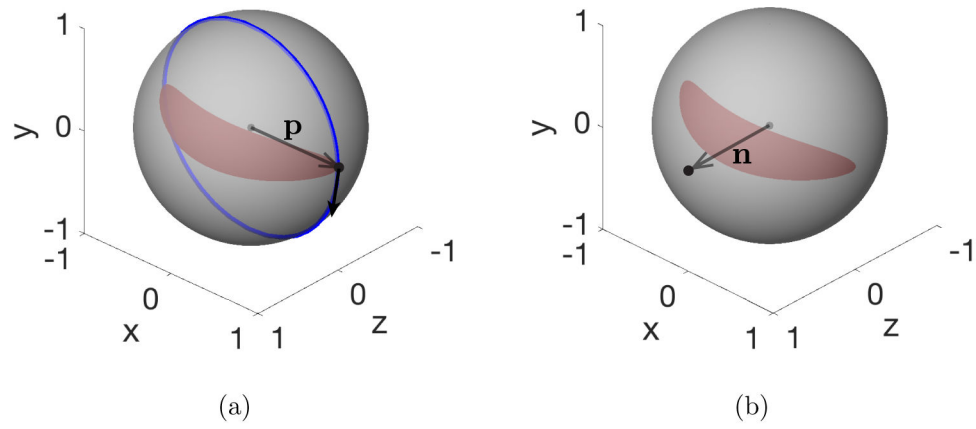


**FIG. 6:** Trajectories of  $\mathbf{p}$  (a) and  $\mathbf{n}$  (b) for a curved prolate capsule with initial orientation  $[\alpha, \beta] = [0, 0]$  at the early stage of simulation ( $0 < \dot{\gamma}t < 500$ ).

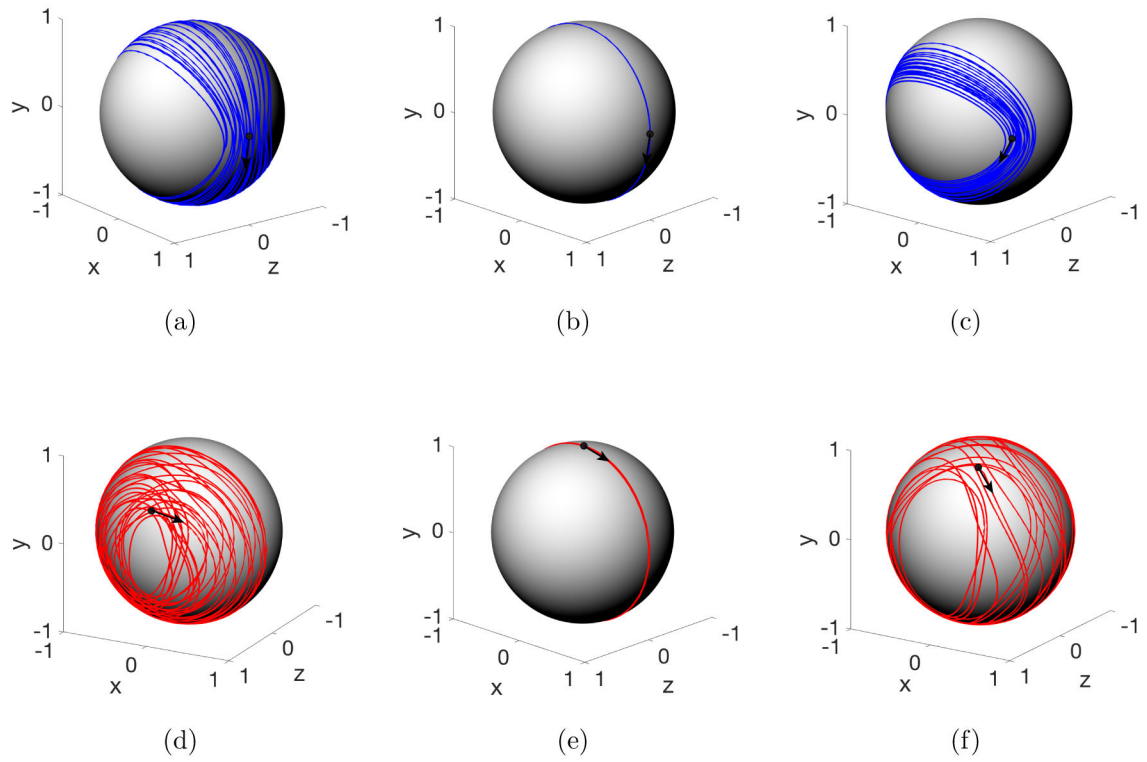


**FIG. 7:** Early-stage trajectories on the unit sphere of the  $\mathbf{p}$  (blue) and  $\mathbf{n}$  (red) vectors of a curved prolate capsule with initial orientation  $[\alpha, \beta] = [0, \pi/6]$  ( $0 < \dot{\gamma}t < 500$ ) (a,d),  $[0, \pi/2]$  ( $0 < \dot{\gamma}t < 100$ ) (b,e), and  $[\pi/6, \pi/3]$  ( $0 < \dot{\gamma}t < 400$ ) (c,f), respectively.

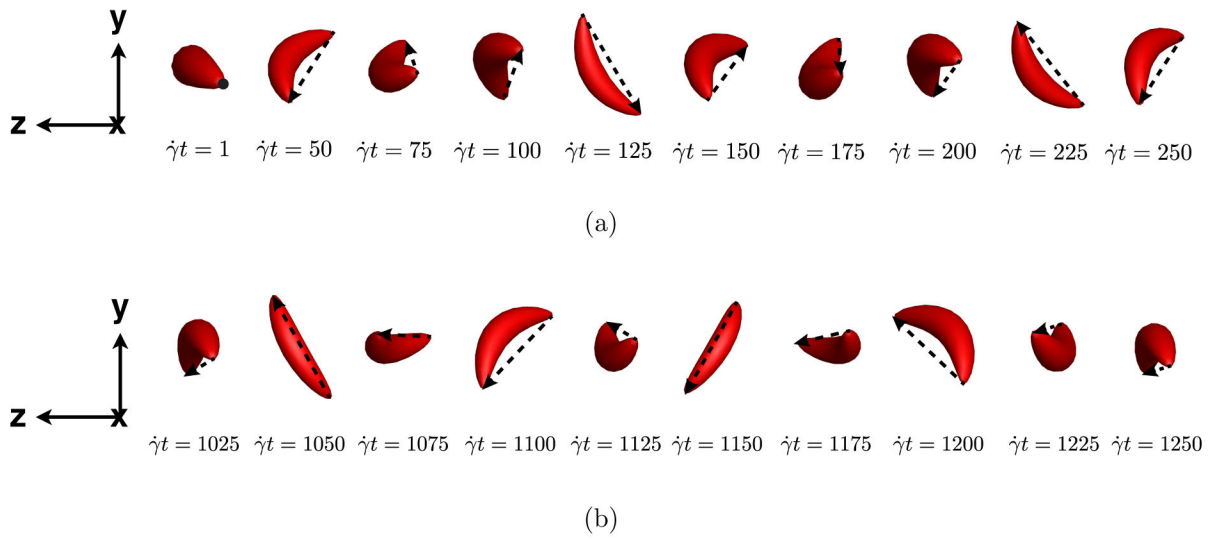


**FIG. 8:** Time sequence images (front view) of the early-stage (a) and long-time (b) motions of a curved prolate capsule with initial orientation  $[\alpha, \beta] = [0, \pi/6]$ . The dashed arrow in each image represents the  $\mathbf{p}$  vector at the corresponding time spot.

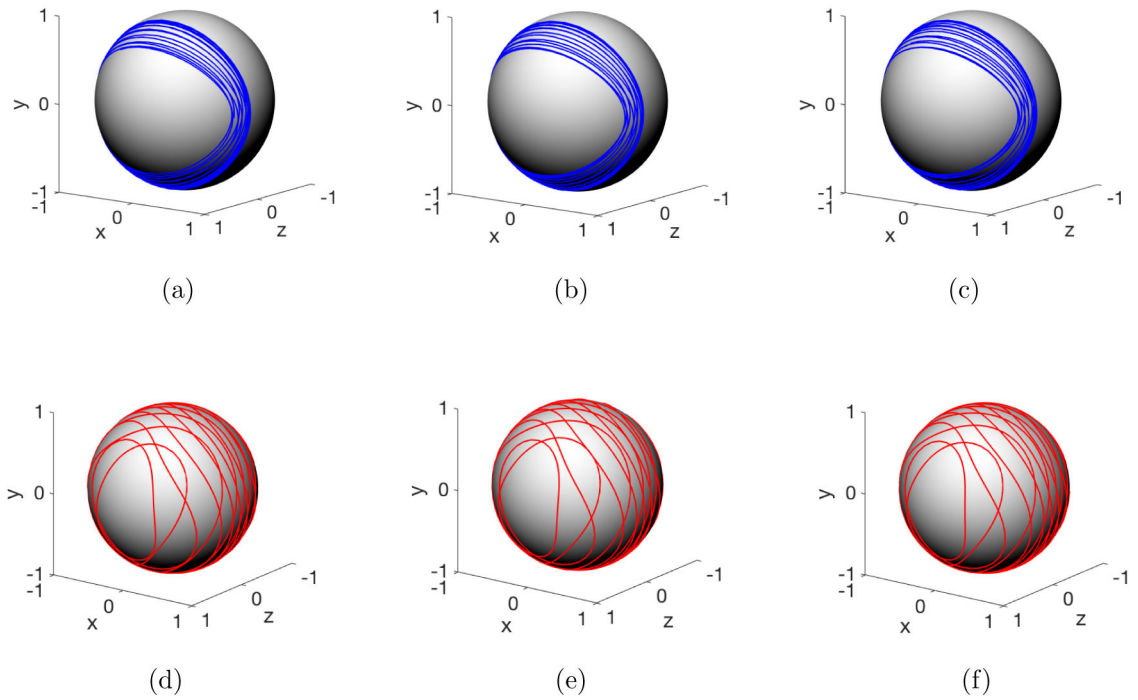
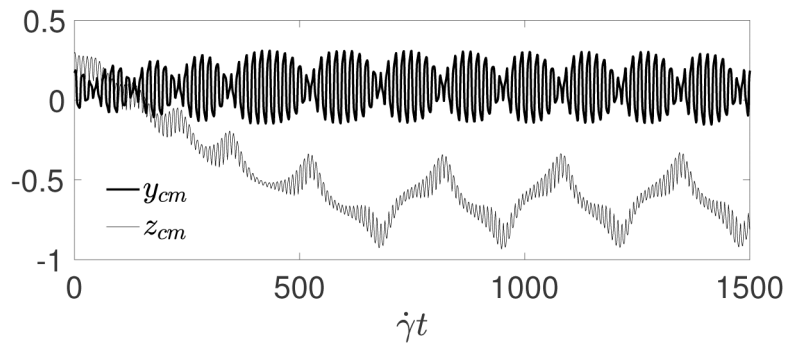
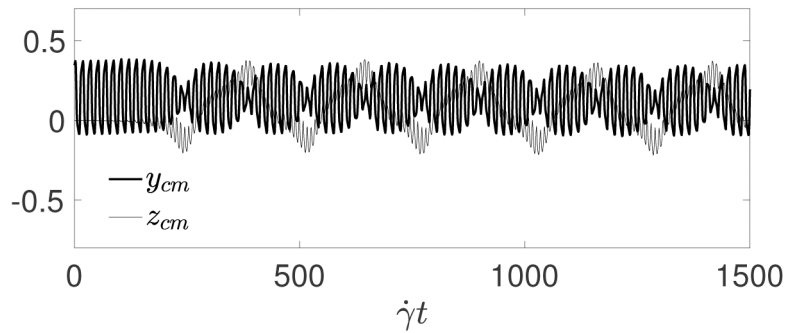


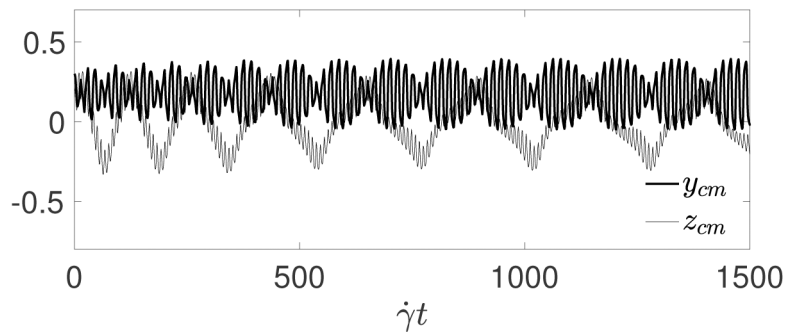
**FIG. 9:** Long-time trajectories on the unit sphere of the  $\mathbf{p}$  (blue) and  $\mathbf{n}$  (red) vectors of a curved prolate capsule with initial orientation  $[\alpha, \beta] = [0, \pi/6]$  (a,d),  $[0, \pi/2]$  (b,e), and  $[\pi/6, \pi/3]$  (c,f), respectively.



(a)



(b)



(c)

**FIG. 10:** Evolution of  $y$ - and  $z$ -components  $y_{cm}$  and  $z_{cm}$  of the center-of-mass position of curved prolate capsules with initial orientations  $[\alpha, \beta] = [0, \pi/6]$  (a),  $[0, \pi/2]$  (b), and  $[\pi/6, \pi/3]$  (c).

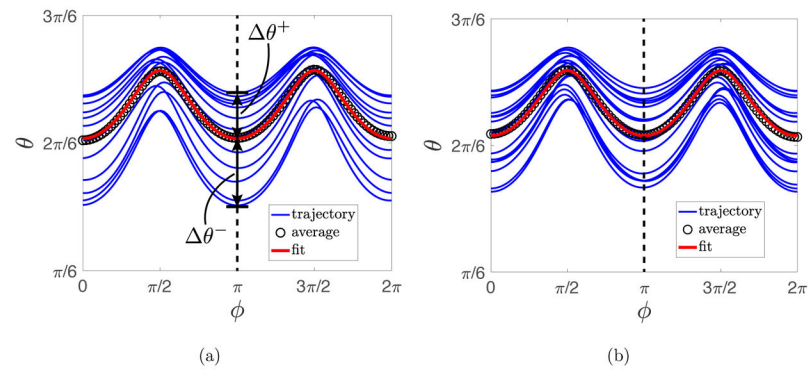


**FIG. 11:** The long-time trajectory (blue curve) of a curved prolate capsule in terms of  $\phi$  and  $\theta$  and the average trajectory (black circles). The red curve represents the fit of the average trajectory using Eq. 11. The black dashed line corresponds to  $\phi = \pi$ .  $\theta^+$  and  $\theta^-$  denote the maximum positive and negative deviations, respectively, of the instantaneous trajectory from the mean when  $\phi = \pi$ . (a)  $Ca = 0.12$ ,  $K = 0.36$ ,  $\lambda = 1$ ; (b)  $Ca = 0.06$ ,  $K = 0.39$ ,  $\lambda = 5$ .

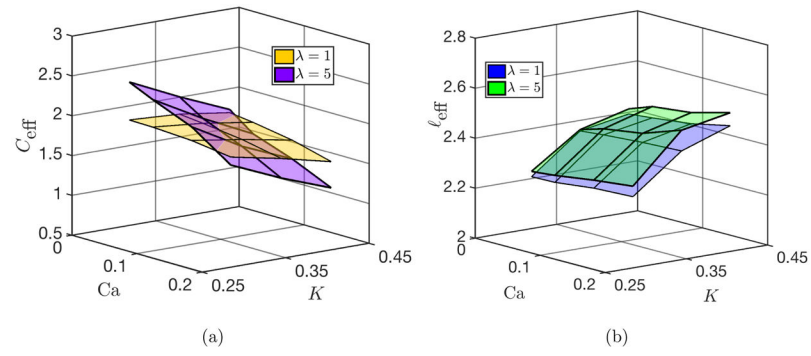


**FIG. 12:** The dependencies of (a) the effective orbit constant  $C_{\text{eff}}$  of the long-time orbit and (b) the effective aspect ratio  $l_{\text{eff}}$  on the deformability  $Ca$  and the degree of curvature  $K$  of the curved prolate capsules.